

# Underwater acoustic surface waves on a periodically perforated metal plate

Thomas J. Graham, Alastair P. Hibbins, J. Roy Sambles, and Timothy A. Starkey<sup>a)</sup>

*Electromagnetic and Acoustic Materials Group, Department of Physics and Astronomy, University of Exeter, Stocker Road, Exeter EX4 4QL, United Kingdom*

(Received 24 June 2019; revised 27 October 2019; accepted 21 November 2019; published online 26 December 2019)

Acoustic surface waves are supported at the surface of appropriately structured elastic materials. Here the excitation and propagation of the lowest-order surface mode supported by a square array of open-ended cavities on a metal plate submerged in water is demonstrated. This mode, which has a half-wavelength character in the cavity, arises due to inter-cavity interaction by evanescent diffraction of the pressure field, and forms a band from zero-frequency to an asymptotic limit frequency. The authors perform an acoustic characterization of the pressure field close to the surface of the perforated plate in the 60–100 kHz frequency range; sound is pulsed from a fixed point-like acoustic source, and the evolution of the acoustic field across the sample surface is measured as a function of time and space with a traversing detector. Using Fourier analysis, the dispersion is imaged between points of high-symmetry ( $\Gamma, X, M$ ) and at planes in momentum-space at fixed frequencies. Beaming of acoustic energy on the surface over a narrow frequency band was observed, caused by the anisotropic mode dispersion of the acoustic surface wave on the square lattice. The measured dispersion shows good agreement with the predictions of a numerical model. © 2019 Author(s). All article content, except where otherwise noted, is licensed under a Creative Commons Attribution (CC BY) license (<http://creativecommons.org/licenses/by/4.0/>).

<https://doi.org/10.1121/1.5139651>

[MRH]

Pages: 4569–4575

## I. INTRODUCTION

Surface waves occur at the boundary between two differing media. There are several different classifications of surface-wave phenomena in acoustics, which include Rayleigh waves,<sup>1</sup> particular cases of Lamb waves,<sup>2</sup> and Scholte-Stoney waves,<sup>3–5</sup> the latter being non-radiative. There are also non-radiative waves called Acoustic Surface Waves (ASWs) that exist on patterned surfaces, where the acoustic wave propagates in the fluid above the solid material.<sup>6</sup> Typically, structures designed to support ASWs take the form of periodic sub-wavelength-sized cavity arrays perforating a solid material. Unlike Lamb waves that can propagate through a material, ASWs exponentially decay in amplitude normal to the structured surface to which they are bound, are highly localized, and have slow group velocity. Structures that support ASWs are particularly interesting because their mode dispersion can easily be tailored by simply changing their structure, and have potential applications in acoustic sensing, energy harvesting, signal processing, and material characterization.<sup>7,8</sup>

Much of the research into ASWs has been undertaken in air.<sup>9–11</sup> Although most studies of underwater structured surfaces have concerned the radiation of Lamb modes influenced by ASWs,<sup>12–14</sup> there have been studies of these non-radiative surface waves over one-dimensional (1D) arrays of water-filled grooves<sup>10</sup> and two-dimensional (2D) arrays of material-filled holes.<sup>15</sup> Furthermore, Hou *et al.* showed that it is possible to excite underwater ASWs over a simple square array of holes in a metal plate,<sup>16</sup> which was assumed to be perfectly rigid.

Typically, patterned surfaces that comprise simple resonating cavities can support localized ASWs. For arrays with sub-wavelength repeat period resonators, these ASWs are non-radiative, existing with in-plane  $k$ -vectors beyond the sound line, defined by  $k_0 = 2\pi f/c$  where  $f$  and  $c$  are the frequency and velocity of a free-space wave. The ASW, caused by the evanescent diffracted fields from the cavities interacting, forms a band from zero-frequency to an asymptotic limit frequency,  $f_{ASW}$ . This limit is the lowest frequency volumetric resonance of the array of holes, where  $f_{ASW}$  depends on the size and shape of the cavity, the spacing between each feature, and the material properties of the solid structure, and the fluid that fills it. In airborne acoustics, where the structure can be considered acoustically rigid to the airborne pressure field,  $f_{ASW}$  can be calculated easily,<sup>16,17</sup> but this is a non-trivial task underwater. However, full-solver computational methods can be used to obtain predictions of the pressure fields, and from these, the dispersion of the ASWs can be calculated.

In this study, a full experimental characterization of the dispersion of the modes supported by a square array of water-filled holes that perforate an aluminum-alloy plate underwater is undertaken. The dispersion of the non-radiative ASW is obtained through Fourier analysis of the pressure fields measured in the fluid close to the surface of the plate. Results demonstrate acoustic beaming of surface wave energy in one direction over a small frequency band. A Finite Element Method (FEM) model that takes into account the full acoustic-elastic interactions of the system is used to confirm and compare to the experimental results. There is good agreement between measured and calculated data for

<sup>a)</sup>Electronic mail: [tg310@exeter.ac.uk](mailto:tg310@exeter.ac.uk)

the full dispersion of acoustic modes in the planes between points of high lattice symmetry in momentum space.

## II. EXPERIMENTAL METHOD

This work investigates an aluminum-alloy plate patterned with a square array of open-ended holes as shown in Fig. 1. A 2D square array of open-ended holes with a radius  $R = 1.5 \pm 0.1$  mm and grating pitch  $\lambda_g = 5.5 \pm 0.1$  mm was drilled through a  $L = 6.4 \pm 0.1$  mm thick plate of aluminum alloy (5083). The plate is  $400 \times 400$  mm in area and has 4900 holes, in a  $70 \times 70$  square array.

Experiments were performed in a  $3.0 \times 1.8 \times 1.2$  m ( $L \times W \times D$ ) water tank, without wall or surface treatments. The alloy plate was hung in a fixed position in the center of the tank with the plate normal parallel to the tank length. The plate was excited with a Neptune Sonar D70 source driven to radiate pulses with the character of Hanning-windowed-sine functions, centered at 70 kHz and with a bandwidth from 50 to 500 kHz.

In order to create a localized point-like source excitation, the source transducer was positioned in a polyvinyl chloride foam enclosure (to provide a pressure-release-like boundary) punctured with a hollow steel tube with an exit diameter of  $6.0 \pm 0.1$  mm (see Fig. 1 schematic). This source modification shielded the transducer from the surrounding water, while providing a highly diffuse, more point-like, radiation pattern from the exit tube. This tube was positioned directly over one of the holes approximately 3 mm from the sample surface. This source geometry provided acoustic fields that can excite the high-momentum surface modes through diffractive coupling, whose wavevectors,  $k_{ASW}$ , are greater than the wavevector of a free-space sound wave,  $k_0 = 2\pi f/c$ .

The near-fields were detected on the opposite side of the sample using a Precision Acoustics  $1.0 \pm 0.1$  mm diameter needle hydrophone mounted on an  $xyz$  spatial scanning stage (in-house built with Aerotech controllers). The tip of the detector was positioned  $0.5 \pm 0.1$  mm from the face of the sample, which is well within the decay length,  $\delta_P$ , of the expected ASW fields ( $\delta_P \approx 40$  mm<sup>18</sup>). The usable frequency range of this source-detector arrangement is between 40 and

100 kHz. A rendering of the underwater setup is shown on the right of Fig. 1.

The experimental data presented in Sec. III were acquired by exciting the sample with the source fixed over a hole at one corner of the sample, position (0, 0), and scanning the detector over a  $106.05 \times 106.05$  mm area, in the  $xy$  plane. The scan steps were  $\Delta x = 1.414$  mm and  $\Delta y = 1.414$  mm, and the signal at each point is an average of 50 repeat pulses to obtain a good signal-to-noise ratio. Each time signal length was 1.3 msec measured at a sampling frequency of 9.4 MHz; this time duration removes any issues that may arise from unwanted tank-wall or surface reflections.

## III. EXPERIMENTAL RESULTS

The measured acoustic pressure field, at an instance in phase, of the wave traveling across the scanned area after being diffracted through the hole at (0, 0) are presented in Fig. 2, as detected voltage (V) in space ( $x$  and  $y$ ). This map shows the acoustic field propagating across the square array of holes, as a function of time,  $t$ , after the pulse was launched. At time  $t = 0.10$  ms the pulse is confined to a region close to the source, and shows the propagation of cylindrical wavefronts, that extend to the edge of the scanned area by the time  $t = 0.15$  ms. At later times  $t = 0.20$  and  $t = 0.25$  ms the ringing of the cavities becomes apparent as the position of the holes become clearly visible in the field data.

Through Fourier analysis of the temporal signals at every spatial point, 2D pressure maps at each frequency are obtained. Example data showing the real pressure amplitude at an instance in phase (instantaneous amplitude), phase, and time-averaged magnitude are depicted in Fig. 3. For the lowest frequency,  $f = 80.0$  kHz (Fig. 3, left panels), the instantaneous amplitude and phase of the wave shows clear cylindrical spreading from the source placed at the bottom left of the scan area. For the two higher frequencies, beaming of acoustic power becomes very evident at an angle of  $45^\circ$  from the  $x, y$  axes, and is highly directional in a confined beam at frequency  $f = 82.7$  kHz.

To gain further insight from the experimental data, the 2D frequency data are Fourier transformed spatially (in  $x$

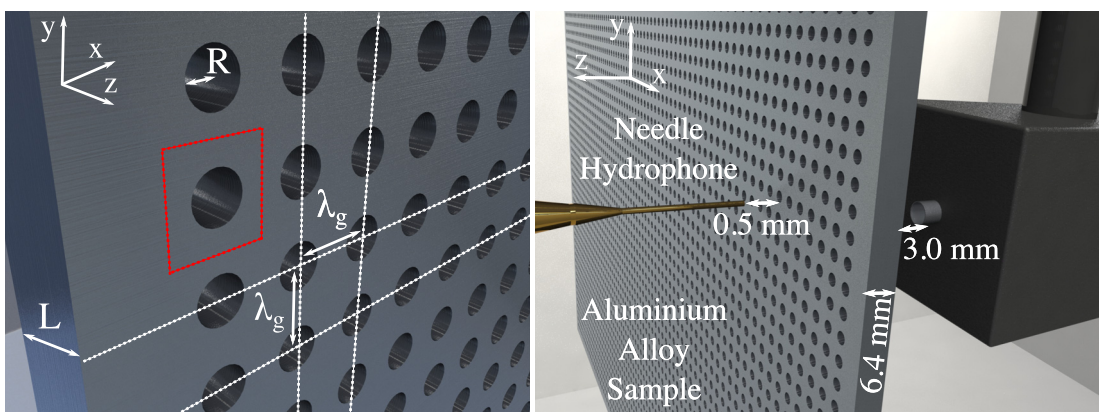


FIG. 1. (Color online) Left: A three-dimensional (3D) rendered image of the square array of holes. The array has cavities of radius,  $R$ , with a pitch,  $\lambda_g$ , in a plate of thickness,  $L$ . The unit cell for this structure is shown as a square red-dotted box. White-dotted lines follow the center lines of selected rows of cavities. Right: A three-dimensional (3D) rendered image of the square array submerged in the water tank. Acoustic pulses are projected from the  $d = 6.0 \pm 0.1$  mm diameter source and detected by a  $1.0 \pm 0.1$  mm diameter needle hydrophone spatially rastered on the opposite sample surface using an  $xyz$  scanning stage.

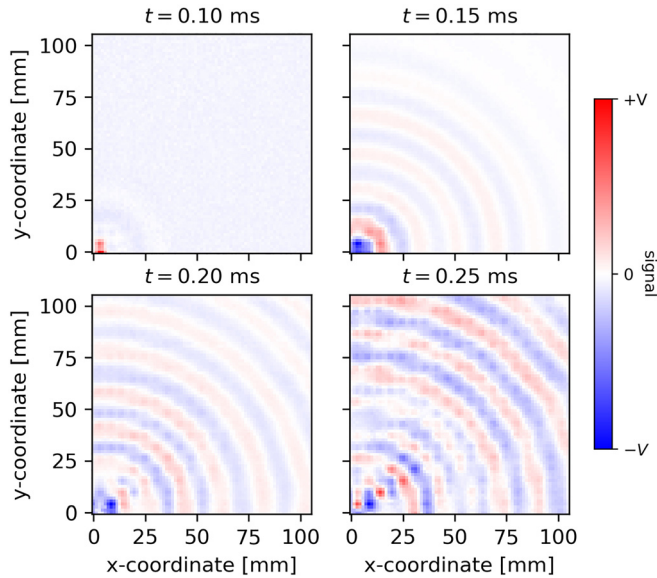


FIG. 2. (Color online) Spatial maps of measured instantaneous voltage (mV) at four different times,  $t=0.10, 0.15, 0.20,$  and  $0.25$  ms, after the source is triggered. The amplitude of the measured signal indicated in the color bar for each time plot presented voltage is  $\pm V=30, 280, 205,$  and  $128$  mV, respectively, for increasing time.

and  $y$ ) after zero-padding ( $\times 3$  factor) in  $x$  and  $y$ . By doing so, the Fourier amplitude as a function of wavevector ( $k_x, k_y$ ) and frequency is obtained, from which the band structure of the surface modes is found between points of high-symmetry ( $\Gamma, X, M$ ) of the reciprocal lattice. Since only one quadrant of the wave propagation is measured with respect to the source ( $+x, +y$ ), once Fourier transformed in space, the dispersion obtained will only show the forward propagation of the mode in one quadrant in reciprocal space ( $+k_x, +k_y$ ).

Figure 4 shows the Fourier amplitude for a plane in  $k$ -space for different frequencies: 75.0, 80.0, 82.7, and 85.0 kHz. In these graphs the sound line, indicated by the solid line, is

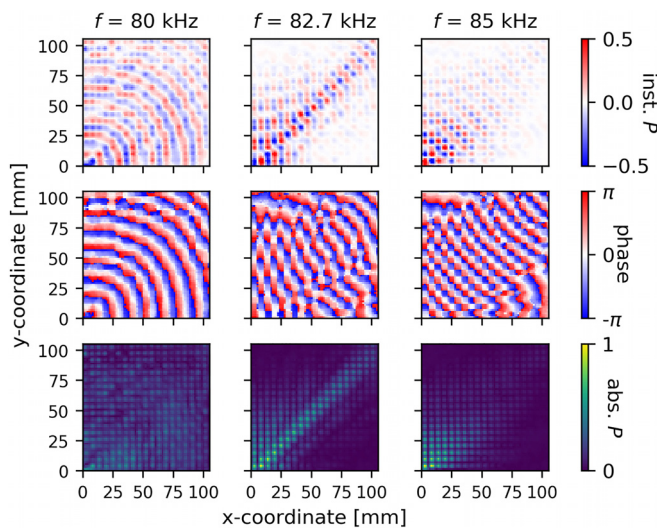


FIG. 3. (Color online) Frequency dependent  $xy$  spatial plots showing the instantaneous real amplitude (top), phase (middle), and time averaged magnitude (bottom) of the measured pressure field above the square array of holes at 80.0, 82.7, and 85.0 kHz. The acoustic beaming across the sample is clearly evident at 82.7 kHz at  $45^\circ$  from the  $x, y$  axis.

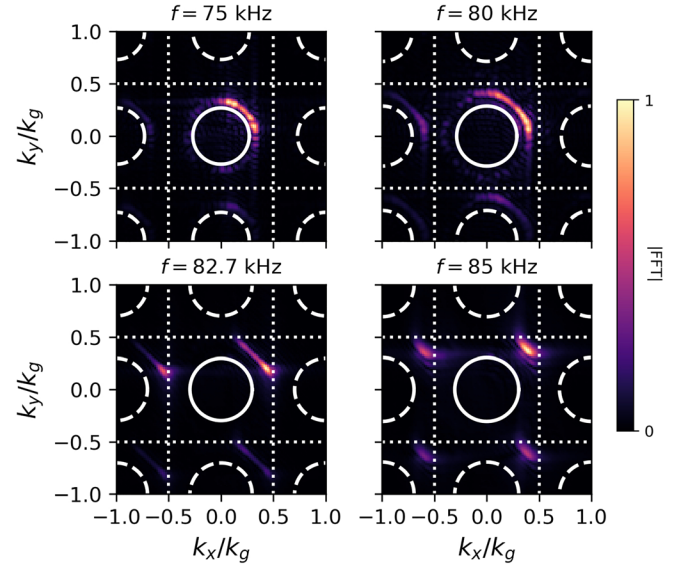


FIG. 4. (Color online) Fourier amplitude plots as a function of wavevector of the field propagating over the square array of holes at frequencies: 75.0, 80.0, 82.7, and 85.0 kHz. The wavevector of a grazing plane wave across the sample surface ( $k_0 = \sqrt{k_x^2 + k_y^2}$ ) is shown as a solid circle: modes beyond this limit are non-radiative (i.e., bound to the surface). Diffracted sound lines are shown as dashed lines. Dotted lines mark the boundary of the first Brillouin zones.

defined by the dispersion of a free-space acoustic wave propagating parallel to the sample surface (a grazing wave), defined by the wavevector,  $k_0$ , of a free-space grazing wave as a function of frequency,  $f$  ( $k_0 = 2\pi f/c$ ). The experimental results show a surface mode beyond the sound line, indicating that mode is indeed bound and has a greater momentum than a grazing wave. As the frequency is increased from 75.0 to 85.0 kHz, the ASW disperses strongly, transforming from a mode that resembles a loosely bound grazing plane wave near the sound line ( $k_{ASW} \approx k_0 = 2\pi f/c$ , where  $c \approx 1500 \text{ ms}^{-1}$ ) to a strongly-confined surface mode ( $k_{ASW} \gg k_0$ ).

The ASW equi-frequency contours begin circular, then become anisotropic as they approach the first Brillouin zone boundary ( $|k_x|, |k_y| = k_g/2$ , where  $k_g = 2\pi/\lambda_g$ ). Since group velocity,  $v_g$ , is defined by  $v_g = \nabla_k \omega$ , where  $\omega$  is the angular frequency, acoustic power transfer is indicated by the direction normal to the mode equi-frequency contour. At 80 kHz, the shape of the ASW contour is approximately circular, meaning power propagates across the sample in all directions. As the frequency increases the contour is perturbed, and at 82.7 kHz the ASW equi-frequency contour has clearly flattened, which corresponds to the beaming of acoustic power across the sample at  $45^\circ$  shown in Fig. 3. And at 85 kHz the surface mode contour has the opposite curvature, which manifests itself as convergent-like phase fronts in the real space pressure maps (Fig. 3).

#### IV. EIGENFREQUENCY ANALYSIS

FEM modeling (COMSOL Multiphysics 5.3) was used to calculate eigenmodes of the bound modes supported by the sample.

The system is modelled as a unit cell bound by Floquet periodic conditions in the  $x$  and  $y$  directions and by Perfectly

TABLE I. Elastic and viscous material parameters for water and aluminum alloy 5083 that are used in the FEM model.  $E$  is the elastic modulus of the material,  $G$  is the shear modulus of the material,  $\rho$  is the density of the material,  $\sigma$  is the Poisson's ratio,  $\mu_B$  is the bulk viscosity, and  $\mu$  is the dynamic viscosity of the medium.

Medium	$E$ (GPa)	$G$ (GPa)	$\rho$ (kg/m <sup>3</sup> )	$\sigma$	$\mu_B$ (mPa s)	$\mu$ (mPa s)
Water	—	—	997.0 ± 0.5 (Ref. 19)	—	2.50 ± 0.46 (Ref. 20)	1.00 ± 0.13 (Ref. 19)
Aluminum alloy	72.0 ± 0.2 (Ref. 21)	26.4 ± 0.2 (Ref. 21)	2660 ± 10	0.34 ± 0.1 (Ref. 21)	—	—

Matched Layers in the  $z$  direction. This approximates the sample as a periodically-perforated plate with infinite extent in the  $x$  and  $y$  direction, bounded top and bottom by water half-spaces which extend infinitely. To fully represent the physical system, the plate is treated as an elastic solid and water as a viscous fluid. This captures the viscous damping in the fluid due to the no-slip boundary condition at the walls of the aluminum plate, which manifests as a negligible reduction in resonance frequency caused by a reduction of the effective velocity of sound in the cavity due to the boundary layer. The elastic and viscous acoustic parameters used in the model for each medium are given in Table I;<sup>19–21</sup> these values are either empirically measured or industry-used estimates of the properties of water and aluminum alloy.

The predicted eigenmodes are compared to experimental results as a function of frequency and wavevector between reciprocal lattice points of high-symmetry in Fig. 5. For the frequency range studied here, the numerical simulations show one ASW mode that lies between 65 and 86 kHz, that moves from  $\Gamma$  to  $X$ ,  $X$  to  $M$ , and  $M$  to  $\Gamma$ , as the in-plane wavevector,  $k_{\parallel} = \sqrt{k_x^2 + k_y^2}$ , moves around the inset of Fig. 5 (where  $X: (k_x, k_y) = (k_g/2, k_y = 0)$ , and  $M: (k_x, k_y) = (k_g/2, k_g/2)$ ). These modes meet the Brillouin zone with zero group velocity, forming standing waves at the  $X$  and  $M$  point. The experimental results agree well with the numerical prediction; showing a surface mode with the same dispersion. We note as the mode group velocity approaches zero, the amplitude of the mode is seen to decrease, which is expected for a wave that is not propagating, and therefore not detected in real space.

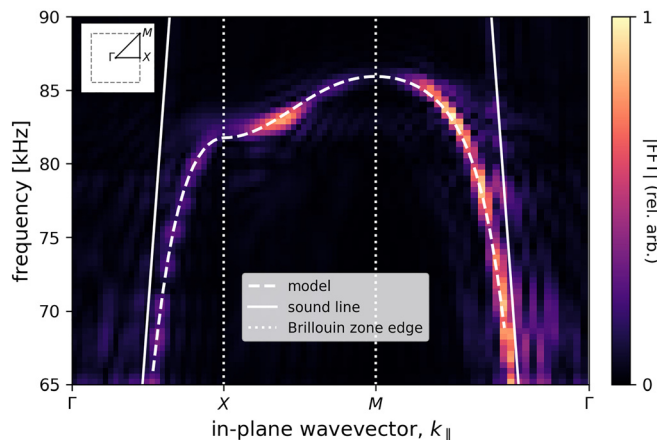


FIG. 5. (Color online) The directional dispersion along planes of high symmetry  $\Gamma - X - M - \Gamma$  of the square array of holes.  $X$ ,  $M$ , and  $\Gamma$  are shown in  $k$ -space in the inset. The crossing between the experimental results and the dashed line at the first Brillouin zone edge,  $X$ , marks the value of the asymptotic frequency,  $f_{ASW} = 81.8$  kHz.

## V. ACOUSTIC AND ELASTIC MODE SHAPES

To investigate the influence of acoustic perturbation on the elastic properties of the plate and the resulting effect on the dispersion of the acoustic surface mode, the deformation of the plate was computationally explored where the mode is at the  $X$  and  $M$  points. Figure 6 shows the mode shapes where pressure is maximum inside the holes of the array, and where the deformation of the surrounding elastic solid is at maximum amplitude at  $X$  and  $M$ . The maximum acoustic pressure in the water for all plots is localized at the center of the holes, which is characteristic of the fundamental mode within the hole.

The deformation at the  $X$  point of reciprocal space is dipolar in nature with maximum deformation in the propagation direction. At the  $M$  point the deformation becomes quadrupolar with deformation maxima in both  $x$  and  $y$  directions. At  $X$ , each neighboring cell pressure field is  $\pi$  radians out-of-phase in the  $x$  direction and at  $M$  in both  $x$  and  $y$ , with the field traveling diagonally. Due to symmetry, at the  $X$  point the unit cell does not deform in the  $y$  direction, and for the  $M$  point it does not distort at the corners of the unit cell.

Interestingly, the asymptotic frequency,  $f_{ASW}$ , calculated for this elastic-solid perforated plate is approximately 4 kHz lower than predicted for the same geometry in a perfectly rigid solid. Figure 7 (left) shows a comparison of the mode dispersion as it approaches the first Brillouin zone boundary at  $X$  calculated for an elastic and for a rigid solid boundary. The ratio of these asymptotic frequencies, at the  $X$  point where the mode is highly localized to the cavity, implies that there is a 4.4% reduction of velocity of sound within the cylindrical cavity, due to the elastic constraint of the boundary walls.

We posit that this slower speed of sound within the water can be understood in terms of the effective compressibility,  $\beta$ , of the fluid, which is in essence increased by the elastic deformation. Since compressibility,  $\beta$ , is related to the bulk modulus,  $B$ , by  $\beta = B^{-1}$  and since  $c = \sqrt{B/\rho}$ , where  $\rho$  is the density of water, the speed of sound in water inside the hole must decrease, reducing the asymptotic frequency of the ASW. A 3.8 kHz change in the frequency as calculated here equates to an  $\approx 9\%$  effective change in the bulk modulus of water.

To validate the plausibility of this difference in ASW asymptotic frequency, and associated slow sound velocity in the water cavity, between elastic and rigid boundary conditions, we compare results to Biot's theory.<sup>22</sup> Biot's theory derives expressions for the solid-fluid mode that exists at the boundary of a fluid cylinder of infinite length bounded by an elastic solid with infinite extent. In Biot's work, the axisymmetric waves that propagate along the cylinder axis are considered, and the ratio of the velocity of sound in the cylinder to the velocity of sound in an unbound fluid ( $\zeta = v/c$ ) is presented as a function

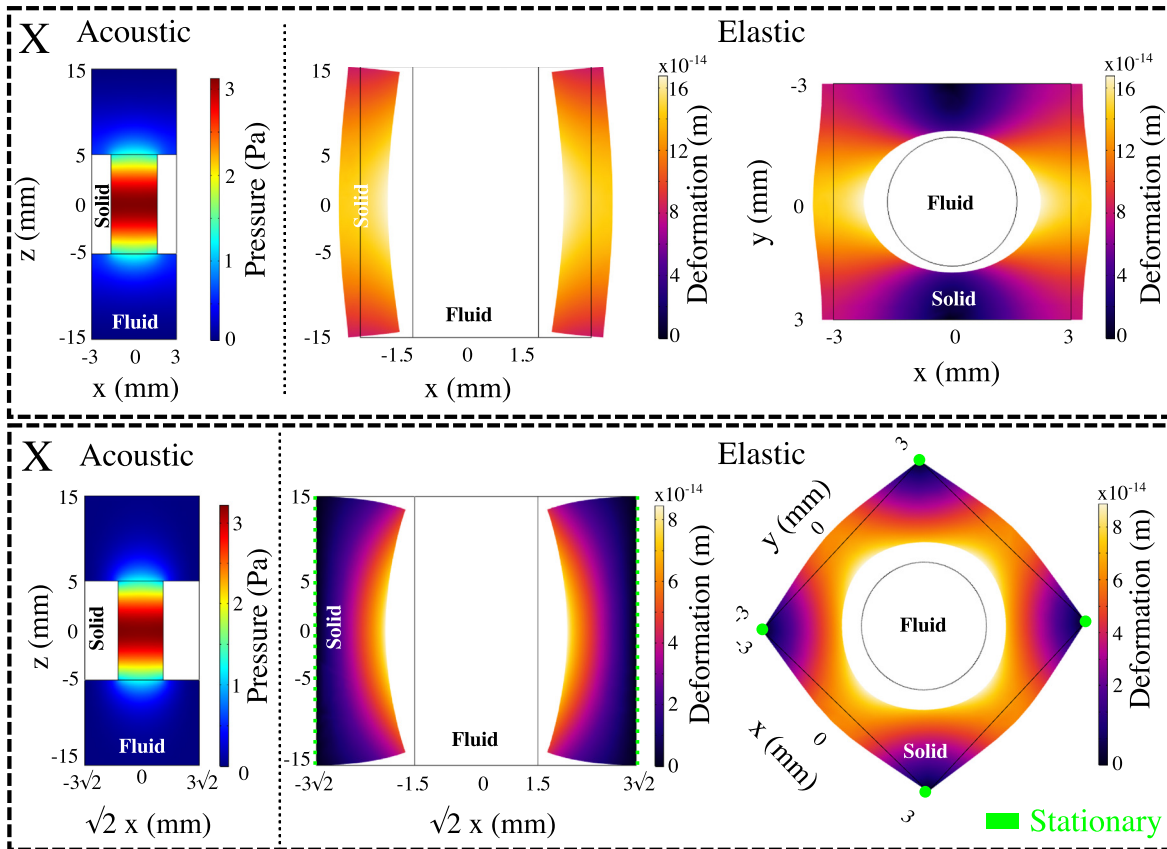


FIG. 6. (Color online) Calculated mode shapes from the FEM model inside one model unit-cell of the square array for an applied pressure of 1 Pa: The acoustic pressure field (left) is plotted on a cross-section through the plate at the center of the fluid cavity, and shows the field is localized in the cavity and decays into the fluid above and below. The elastic deformation shape and magnitude (color scale) of the solid (middle and right) are plotted in the solid region. The middle plots show a cross-section through the thickness of the plate at the cavity center, and the right plots show a cross-section taken at the mid-plane of the plate thickness. The top section through the plate thickness (left, middle) are cross-sections shown as a function of  $x$  with  $y = 0$  mm, while the bottom are shown where  $x = y$ ; these correspond to the ASW propagation directions in real space at the  $X$  and  $M$  point, respectively. The displacement has been enhanced by  $\times 10^9$  to aid visualization.

of the dimensionless wavelength parameter  $\lambda/D$  where  $D$  is the cylinder diameter (see Appendix A for further details).

Following Biot's presentation, Fig. 7 (right) shows this theory calculated using the physical parameters for water and

aluminum detailed in Table I. At short wavelength the velocity ratio,  $\zeta$ , is close to unity; as the wavelength increases the velocity ratio decreases before tending to a limit velocity,  $v_{\text{limit}}$ , dictated by the fluid density,  $\rho$ , and solid shear modulus,  $G$ .

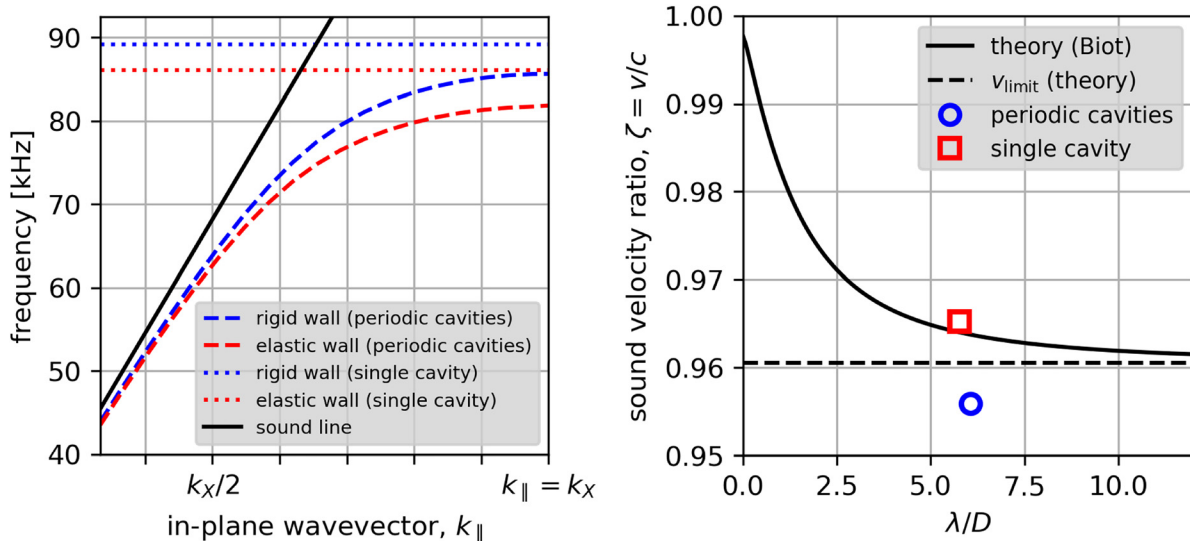


FIG. 7. (Color online) Theoretical and numerical results comparing the difference between an elastic and rigid solid. (Left) FEM calculated dispersion relation for elastic and rigid solid for a periodic array of resonant cavities, compared to the resonance calculated for a cavity in a plate with infinite extent in the plane (not periodic). (Right) A comparison of sound velocities calculated using Biot's theory and numerical model sound velocities for the periodic and infinite cavity system.

For comparison to Biot's theory, the resonance frequency of a single cavity in an elastic ( $f_e$ ) and in a rigid ( $f_r$ ) plate for the same sample thickness and with infinite extent is calculated. From this, the ratio of velocities are obtained ( $v/c = f_e/f_r$ ) and plotted at appropriate  $\lambda/D$  in Fig. 7 (right). The sound velocity ratio shows good agreement between Biot's theory and the numerical simulation; the slight underestimation in the velocity reduction of the numerical model is expected since cavity end-effects will increase the effective compressibility of the fluid in the cavity—not present for Biot's infinite cylinder of fluid.

The same approach is used to compare the sound velocity ratio for the periodic cavity array, studied experimentally, at the  $X$ -point in mode dispersion; again the FEM velocity ratio agrees with Biot's theory within 1%, but this time the reduction in velocity of sound in the fluid cavity is overestimated. This is unsurprising, since perforating an elastic plate will only enhance the elastic deformation of the cavity walls (see Fig. 6).

## VI. CONCLUSIONS

We have observed underwater ultrasonic ASWs supported by a square array of open-ended holes in a perforated aluminum plate. By Fourier analyzing the fields temporally and spatially, we characterized the ASW and obtained its dispersion. In addition, in-plane ultrasonic beaming was observed over a narrowband of frequencies, centered around 82.7 kHz. The experimental results presented agree well with numerical simulations. A Poisson's ratio of 0.34 and elastic modulus of 72.0 GPa resulted in an asymptotic frequency (at the  $X$  point) change of  $\approx 4$  kHz compared to that of an equivalent rigid system. This frequency reduction is attributed to an increase in the effective compressibility of the fluid within the cavities, as is seen in Fig. 6, because the cavity walls now act as an elastic constrain. The ultrasound technique presented could be applied to any submerged flat 2D system to detect ASWs over periodic arrays of diffracting structures. By adding extra degrees of freedom or changing the geometry of the array these surfaces can be readily tailored to support ASW modes tuned to selected frequency ranges. Acoustic devices made from such 2D arrays could be used to harvest directional energy, improve acoustic propagation for communications, or direct unwanted sound away from an area.

## ACKNOWLEDGMENTS

We acknowledge financial support from the Engineering and Physical Sciences Research Council (EPSRC) of the United Kingdom, via the EPSRC Centre for Doctoral Training in Metamaterials (Grant No. EP/L015331/1) and Thales UK through an Industrial CASE Training Account (Voucher No. 14440030). T.A.S. acknowledges the financial support of DSTL. All data created during this research are openly available from the University of Exeter's institutional repository at <https://ore.exeter.ac.uk/repository/>.

## APPENDIX A: THEORY FOR ACOUSTIC MODE DISPERSION IN A FLUID CONSTRAINED BY AN ELASTIC CONSTRAINT

The results presented in Fig. 7 are produced from the theory presented in Biot's 1952 article "Propagation of Elastic Waves in a Cylindrical Bore Containing Fluid."<sup>22</sup> Following Lamb's work<sup>23</sup> for large wavelength, Biot derives a more general theory for axisymmetric acoustic and elastic waves propagating down the axis, either in or at the boundary, of a fluid-filled cylinder bound by an elastic solid with infinite extent. The dispersion relations of these modes are derived, and it is shown that only one wave is caused solely by the coupling of fluid and liquid, and is termed the Stoneley wave (which is more commonly recognized as the Scholte wave).

The following equations are included for completeness, and we refer the reader to the original work for the full derivation. The results presented are obtained by numerically solving the following equation [corrected from Eq. (3.14) in Biot<sup>22</sup>],

$$4(1 - \zeta_1^2)^{1/2} \left[ \frac{1}{ka} + \frac{K_0(ka)}{K_1(ka)} \right] - \frac{2(2 - \zeta_1^2)(1 - \zeta_2^2)^{1/2}}{ma} - \frac{(2 - \zeta_1^2)^2 K_0(ma)}{(1 - \zeta_2^2)^{1/2} K_1(ma)} = \frac{\rho_f}{\rho_s} \frac{\zeta_1^4}{(1 - \zeta^2)^{1/2}} \frac{I_0[la(1 - \zeta^2)^{1/2}]}{I_1[la(1 - \zeta^2)^{1/2}]}, \quad (\text{A1})$$

where  $\zeta$  is considered to be the unknown variable, and defined as  $\zeta = v/c$  the ratio of fluid phase velocity to the velocity of sound in an unbound fluid.  $\rho_s$  and  $\rho_f$  denote the density of the solid and the fluid, respectively,  $D$  is the diameter of the fluid cylinder, and  $\lambda$  is the wavelength in fluid.  $I$  and  $K$  denote the modified Bessel function of the first kind of real order, and the modified Bessel function of the second kind, respectively.  $\zeta$  is also related to the other terms:  $\zeta_1 = c\zeta/v_s$  and  $\zeta_2 = v_s\zeta_1/v_c$ , where  $v_c$  and  $v_s$  are the compressional and shear velocities of sound in the solid, and are related to the following:

$$ka = \frac{\pi D}{\lambda} (1 - \zeta_1^2)^{1/2}, \quad ma = \frac{\pi D}{\lambda} (1 - \zeta_2^2)^{1/2}. \quad (\text{A2})$$

The shear wave speed is obtained from the shear modulus,  $G$ , and density of the solid,  $\rho_s$ , by  $v_s = \sqrt{G/\rho_s}$ , from which the compressional wave speed is determined with the Poisson ratio,  $\nu$ :

$$v_c = v_s \sqrt{\frac{2(1 - \nu)}{1 - 2\nu}}. \quad (\text{A3})$$

The long wavelength velocity ratio limit shown by the dotted line in Fig. 7 is given by

$$\frac{v}{c} = \frac{1}{[1 + (\rho_s c^2 / G)]^{1/2}}. \quad (\text{A4})$$

The material properties used are shown in Table I, and the velocity of sound is assumed to be  $c = 1490 \text{ ms}^{-1}$ .

- <sup>1</sup>Lord Rayleigh, "On waves propagated along the plane surface of an elastic solid," *Proc. London Math. Soc.* **1**, 4–11 (1885).
- <sup>2</sup>H. Lamb, "On waves in an elastic plate," *Proc. R. Soc. London A* **93**, 114–128 (1917).
- <sup>3</sup>P. Hess, "Surface acoustic waves in materials science," *Phys. Today* **55**(3), 42–47 (2002).
- <sup>4</sup>J. G. Scholte, "The range of existence of Rayleigh and Stoneley waves," *Mon. Not. R. Astron. Soc.* **5**, 120–126 (1947).
- <sup>5</sup>R. Stoneley, "The effect of the ocean on Rayleigh waves," *Geophys. J. Int.* **1**, 349–356 (1926).
- <sup>6</sup>Z. He, H. Jia, C. Qiu, Y. Ye, R. Hao, M. Ke, and Z. Liu, "Nonleaky surface acoustic waves on a textured rigid surface," *Phys. Rev. B*, **83**, 132101 (2011).
- <sup>7</sup>T. Matikas and D. Aggelis, "New trends in materials: Nondestructive characterization using Surface Acoustic Wave methodologies," in *Ultrasonic Waves*, edited by A. Antunes dos Santos, Jr. (IntechOpen, Rijeka, Croatia, 2012), Chap. 13.
- <sup>8</sup>M. Oudich and Y. Li, "Tunable sub-wavelength acoustic energy harvesting with metamaterial plate," *J. Phys. D: App. Phys.* **50**, 315104 (2017).
- <sup>9</sup>R. J. Donato, "Model experiments on surface waves," *J. Acoust. Soc. Am.* **63**, 700–703 (1978).
- <sup>10</sup>L. Kelders, J. F. Allard, and W. Lauriks, "Ultrasonic surface waves above rectangular-groove gratings," *J. Acoust. Soc. Am.* **103**, 2730–2733 (1998).
- <sup>11</sup>K. M. Ivanov-Shits and F. V. Rozhin, "Investigation of surface waves in air," *Sov. Phys. Acoust.* **5**, 510–512 (1959).
- <sup>12</sup>H. Estrada, V. Gómez-Lozano, A. Uris, P. Candelas, F. Belmar, and F. Meseguer, "Sound transmission through plates perforated with two periodic subwavelength hole arrays," *J. Phys. Condens. Matter.* **23**, 135401 (2011).
- <sup>13</sup>H. Estrada, P. Candelas, A. Uris, F. Belmar, F. Meseguer, and F. J. García de Abajo, "Sound transmission through perforated plates with subwavelength hole arrays: A rigid-solid model," *Wave Mot.* **48**, 235–242 (2011).
- <sup>14</sup>M. Mazzotti, M. Miniaci, and I. Bartoli, "Band structure analysis of leaky Bloch waves in 2D phononic crystal plates," *Ultrasonics* **74**, 140–143 (2017).
- <sup>15</sup>H. Estrada, P. Candelas, F. Belmar, A. Uris, F. J. García De Abajo, and F. Meseguer, "Engineering surface waves in flat phononic plates," *Phys. Rev. B* **85**, 174301 (2012).
- <sup>16</sup>B. Hou, J. Mei, M. Ke, W. Wen, Z. Liu, J. Shi, and P. Sheng, "Tuning Fabry-Perot resonances via diffraction evanescent waves," *Phys. Rev. B*, **76**, 054303 (2007).
- <sup>17</sup>X. Wang, "Theory of resonant sound transmission through small apertures on periodically perforated slabs," *J. Appl. Phys.* **108**, 064903 (2010).
- <sup>18</sup>L. E. Kinsler, A. R. Frey, A. B. Coppens, and J. V. Sanders, *Fundamentals of Acoustics*, 2nd ed. (Wiley, New York, 2000).
- <sup>19</sup>J. Vennard and R. Street, *Elementary Fluid Mechanics*, 5th ed. (Wiley, New York, 1975).
- <sup>20</sup>M. J. Holmes, H. G. Parker, and M. J. W. Povey, "Temperature dependence of bulk viscosity in water using acoustic spectroscopy," *J. Phys.* **269**, 012011 (2011).
- <sup>21</sup>J. M. Holt, C. Gibson, and C. Y. Ho, *Structural Alloys Handbook* (Purdue University, Indiana, 1996), Vol. 2.
- <sup>22</sup>M. A. Biot, "Propagation of elastic waves in a cylindrical bore containing a fluid," *J. Appl. Phys.* **23**, 997–1005 (1952).
- <sup>23</sup>H. Lamb, "On the velocity of sound in a tube, as affected by the elasticity of the walls," *Mem. Proc. Manchester Lt. Philos. Soc.* **XIII**(9), 1–16 (1898).